Title

Effect of design on the performance of steel–alumina bilayers and trilayers subject to ballistic impact

Journal

Mechanics of Materials, 91(P1)

ISSN

0167-6636

Authors

Holland, Chance C
Gamble, Eleanor A
Zok, Frank W
et al.

Publication Date

2015-12-01

DOI

10.1016/j.mechmat.2015.05.002

Peer reviewed

Mechanics of Materials 91 (2015) 241–251

Contents lists available at ScienceDirect

Mechanics of Materials

journal homepage: www.elsevier.com/locate/mechmat

Effect of design on the performance of steel–alumina bilayers and trilayers subject to ballistic impact

Chance C. Holland [a,b,*], Eleanor A. Gamble [a], Frank W. Zok [a], Vikram S. Deshpande [c], Robert M. McMeeking [a,b,d]

[a] Materials Department, University of California, Santa Barbara, CA 93106, USA
[b] Mechanical Engineering Department, University of California, Santa Barbara, CA 93106, USA
[c] Department of Engineering, University of Cambridge, Cambridge CB2 1PZ, UK
[d] School of Engineering, University of Aberdeen, King's College, Aberdeen AB24 3UE, UK

ARTICLE INFO

Article history:
Received 23 October 2014
Received in revised form 1 May 2015
Available online 14 May 2015

Keywords:
Design
Penetration resistance
Impact
Trilayer
Energy absorption
Damage

ABSTRACT

Composite armors systems containing ceramic components are capable of offering greater ballistic protection than those of monolithic metals alone. The level of protection afforded by a composite armor depends sensitively on the materials utilized and their spatial configuration. Using numerical simulation, we investigate the effects of relevant design parameters on the ballistic performance of thin, unbonded ceramic–metal bilayers and trilayers subject to normal impact by steel spheres. The deformation behavior of the constituent phases is described by established constitutive laws. The predictive capability of the numerical model is validated through comparisons of simulation results with experimental measurements of displacement profiles of the back facesheet of a reference trilayer. The simulation results indicate that the ceramic–metal bilayer with the ceramic at the impact side offers the highest ballistic resistance; removing metal from the rear of the structure and placing it on the impact side (forming a trilayer) results in reduced ballistic resistance. Additionally, the onset of target penetration is found to correlate with high levels of energy dissipated within the target. The implication is that composite armors should be designed to maximize the energy dissipated in the projectile, not in the armor. Accordingly, effective designs at resisting failure are found to have high ceramic-to-metal mass ratios, with a finite (though small) amount of metal on the back face.

1. Introduction

Armor systems containing ceramic components can significantly outperform monolithic metals of equivalent areal density (mass per unit area) (Wilkins et al., 1967; Wilkins, 1978; Hetherington and Rajagopalan, 1991; Hetherington, 1992). Their performance depends on not only the intrinsic properties of the constituent materials but also on the relative amounts of ceramic and metal and their spatial arrangement. For applications involving military ground vehicles, the armors must be designed to protect against a range of projectile threats and be lightweight, to maintain vehicle maneuverability, load-carrying capacity and fuel efficiency. In the present study, numerical simulations with established constitutive laws for the constituent materials are used to investigate the effects of design on ballistic performance of model composite armors comprising layers of ceramic and metal. Comparisons are made on the basis of equivalent areal density.

* Corresponding author at: Materials Department, University of California, Santa Barbara, CA 93106, USA. Mobile: +1 (805) 708 4106.
E-mail address: chance.holland@gmail.com (C.C. Holland).

http://dx.doi.org/10.1016/j.mechmat.2015.05.002
0167-6636/

High-performance ceramics are attractive in armor applications because of their low density, high hardness and high compressive strength. Furthermore, at sufficiently high strain rates, their strength is highly strain rate sensitive, exhibiting increases above quasi-static values. The dynamic strengthening has been attributed to a combination of material confinement, derived either from geometrical or inertial effects, and inherent limitations of crack speed. However, because of their brittleness under tensile loadings, ceramics in armors must be backed by stiff, tough materials, *e.g.,* steels or fiber-reinforced polymer composites.

The advent of modern lightweight composite armor is attributable to the pioneering work of Wilkins and co-workers (Wilkins et al., 1967; Wilkins, 1978) on penetration mechanisms of bonded ceramic–metal bilayers. Through a combination of experiments and numerical simulations, they identified some of the key mechanisms operative during an impact event and the armor characteristics that yield good ballistic resistance. First, the high compressive strength of the ceramic results in large impact stresses that exceed the yield strength of the (metallic) projectile. This leads to blunting and lateral deformation of the projectile and a concomitant reduction in interface stresses. Second, a conoid of damaged material develops at the impact site and extends to the backing plate. The conoid effectively spreads the impact load over an increased area such that the stresses at the back plate can be accommodated by plastic deformation of the plate without rupture. These studies also revealed that the reflection of the initially-compressive stress wave from the ceramic–metal interface results in high tensile stresses that can lead to comminution of the ceramic directly beneath the impact site. Additionally, at sufficiently high velocities, comminution leads to the formation of a cylindrical plug of heavily-damaged material with a diameter roughly equal to the projectile diameter. Subsequent penetration of the back facesheet can occur either by a localized shear plugging mechanism or by radial cracking and petalling, depending on the thicknesses of the two plates and the severity of the ballistic threat. Additional details of the effects of design on the ballistic performance of ceramic–metal bilayers were subsequently investigated by a number of other researchers (Hetherington, 1992; Shi and Grow, 2007; Ben-Dor et al., 2000, 2005, 2009; Fawaz et al., 2006; Zaera and Sánchez-Gálvez, 1998).

The objectives of the present study are to improve upon the understanding of the mechanics of dynamic impact of multilayered composites and to identify design principles for lightweight, penetration resistant systems. This is accomplished by examining deformation and failure of thin, layered ceramic–metal composites during impact by spherical projectiles. The study is based largely on a parametric finite element (FE) study of impact of a family of bilayers and trilayers with equivalent areal density. The targets are characterized by two dimensionless parameters: the ceramic-to-metal mass ratio $\bar{m}$ and the front-to-back metal facesheet thickness ratio $\bar{t}$. The work on trilayers is motivated by the recognition that metallic facesheets may be used for the purpose of protecting the underlying ceramic layer from in-service wear and to improve multi-hit capability (Sarva et al., 2007) by containing comminuted ceramic debris in the vicinity of impact. Note, we do not consider bonded interfaces between the layers of the target system. The elastic/plastic response of the constituents is modeled using established constitutive laws: the Johnson–Cook model for metals (Johnson and Cook, 1983, 1985; Dey et al., 2007; Zerilli and Armstrong, 1987; Bao and Wierzbicki, 2004) and the Deshpande–Evans model for ceramics (Deshpande and Evans, 2008; Deshpande et al., 2011). Calibration and validation of the ceramic model has recently been completed, using a variety of tests, including quasistatic indentation (Gamble et al., 2011), impact of confined ceramic tiles (Compton et al., 2013) and projectile penetration of ceramic–metal trilayers (Gamble et al., 2013). In the present study, ballistic performance is characterized by two metrics: (i) the peak permanent back face deflection of the target and (ii) the point at which failure initiates within the rear metal layer. Failure initiation is described by a critical strain criterion. Previous studies have employed analogous metrics (specifically, on the basis of target deflection) to characterize ballistic performance (Goncalves and De, 2004; Lopez-Puente et al., 2005).

The article is organized in the following way. First, the pertinent model details – including the FE model, the material constitutive laws and the nature of the parametric study – are presented. The predictive capability of the model is demonstrated through comparisons of predicted back-face deformation profiles with those measured on a reference steel–alumina trilayer (reported elsewhere Gamble et al., 2013). The numerical results of the parametric study are then presented in the form of contour maps of deflections in the $\bar{m}$–$\bar{t}$ design space at prescribed impact velocities. Complementary analyses of impact stresses and energy dissipation are also presented, as needed to glean insights into the effects of target design. We find that the bilayer offers the best ballistic performance; that is, removing metal from the back facesheet and adding it to the front face (forming a trilayer) invariably leads to a reduction in ballistic performance. Furthermore, beyond a critical (moderate) value of $\bar{m}$, the performance of the bilayer becomes remarkably insensitive to further changes in $\bar{m}$. Failure is found to correlate with high levels of energy dissipation in the target, indicating that failure-resistant target designs should maximize the energy dissipated *in the projectile*, thereby minimizing the energy that must be dissipated in the target.

2. Numerical methods and material models

A numerical study was performed to investigate the effects of design of a model armor system on ballistic performance. The test geometry and the material models used in the present study can be found in a preceding article by Gamble et al. (2013); a synopsis of the relevant details and subtle differences from the previous study are presented below. In the experiments, spherically-shaped projectiles were used eliminate the potential for projectile yaw.

Consistent with the experiments, our numerical study considers only spherical projectiles. All target geometries have equivalent areal density.

2.1. FE model: geometry, materials, mesh and boundary conditions

Finite element (FE) calculations of the impact tests were performed on a 2-D axisymmetric model using Abaqus Explicit v6.9-EF1. The geometry, materials, mesh and boundary conditions used in the impact test simulations are shown in Fig. 1. The trilayer targets comprise front and back facesheets of 4130 steel and an intervening tile of an armor-grade alumina (Corbit 98, Bitossi Industries). In the case of bilayers, the front facesheet is absent and the projectile impacts directly onto the ceramic. The thicknesses of the front facesheet ($t_{m,f}$), the ceramic layer (t_c) and the back facesheet ($t_{m,b}$) are selected in accordance with the prescription given in Section 2.4 (Eqs. (5)–(7)). The targets are clamped between 12.7 mm-thick ring-plates of A2 tool steel. Fixed displacement boundary conditions are used on the outer edge of the clamping structure. In all cases, the projectile is a 304 stainless steel sphere with a diameter of $2R = 7.14$ mm and a mass of 1.49 g. All FE meshes utilize four-noded, bilinear, reduced-integration elements. A graded unstructured mesh is used for the projectile; the element size is gradually increased from 200 μm ($\sim R/18$) at the impact site to 800 μm ($\sim R/4.5$) at the trailing edge. A structured mesh is used in the target layers. A 100 μm element size is used in the front facesheet near the impact site; the element width is increased to 200 μm at a distance of 8 mm from the symmetry axis. Both the ceramic tile and the back facesheet are uniformly meshed with 200 μm elements; this element size was selected on the basis of a mesh sensitivity study, wherein further reductions in element size were found not to have a significant effect on the simulation results, particularly the back face deflection and the extent of damage in the ceramic layer. The clamping plates are represented by an unstructured mesh with 700 μm elements and are treated as being elastic with properties provided in Table 1. Interactions between materials are modeled using a kinematic contact algorithm. The interfaces between the various components are unbonded, as in the experiments. Coulomb friction with coefficient 0.2 is used for all contacts. Mass scaling is not employed in these calculations.

2.2. Constitutive laws

2.2.1. Projectile

A non-damaging Johnson–Cook (1985) constitutive law is used for the projectile. The model accounts for strain hardening, rate sensitivity and thermal softening. The flow stress σ_0, as implemented in Abaqus, is given by:

Table 1
Properties of the projectile and confining fixture (from Stout and Follansbee (1986)).

Property	304 Steel	A2 tool steel
ρ (kg/m^3)	7800	7800
E (GPa)	200	200
ν	0.3	0.3
A (MPa)	1100	–
B (MPa)	610	–
C	0.013	–
$\dot{\varepsilon}_o$ (1/s)	1	–
n	0.4	–
m	0.82	–
T_{room} (K)	300	–
T_{melt} (K)	1800	–
c_p(J/(kg K))	450	–

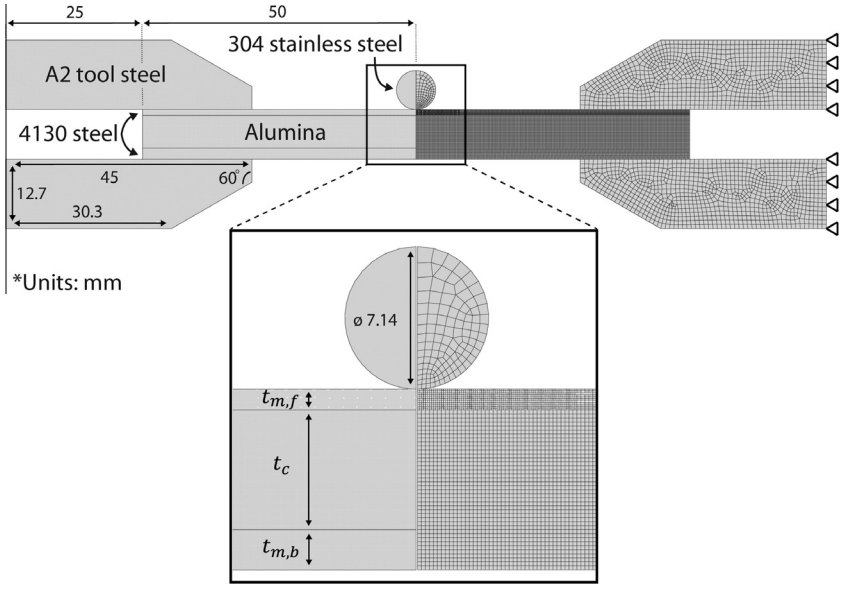

Fig. 1. Schematics of the impact simulations. Left: geometry and materials. Right: finite element mesh and boundary conditions.

$$\sigma_0 = \left[A + B(\bar{\varepsilon}^{pl})^n\right]\left[1 + C\ln\left(\frac{\dot{\bar{\varepsilon}}^{pl}}{\dot{\varepsilon}_0}\right)\right](1 - \hat{\theta}^m) \quad (1)$$

where

$$\hat{\theta} = \frac{T - T_{room}}{T_{melt} - T_{room}}. \quad (2)$$

Here, A is the initial yield stress at a reference strain rate $\dot{\varepsilon}_0 = 1\ s^{-1}$, B is a strain hardening constant, $\bar{\varepsilon}^{pl}$ is the equivalent plastic strain, n is the strain hardening exponent, C is a strain-rate sensitivity constant, $\hat{\theta}$ is the dimensionless temperature, m is the thermal softening exponent, and T is the absolute temperature. The yield stress of the steel balls was inferred by compressing the balls between ceramic platens to varying load levels and measuring the resulting permanent contact area (Gamble et al., 2013). Other properties were obtained from the literature (Stout and Follansbee, 1986) (Table 1). Under dynamic adiabatic conditions, 90% of the energy from plastic deformation is assumed to be converted into heat. Damage and failure are omitted from the material model to prevent artificial mass loss. Although some fragmentation of the projectile has been observed in previous experiments, it occurs only after the projectile has undergone large plastic deformation. Thus it is not expected to significantly affect the transmitted loads in the early (relevant) stages of impact.

2.2.2. Steel layers

The 4130 steel layers are also represented by the Johnson–Cook constitutive law (Eqs. (1) and (2)). However, as we discuss below, two sets of calibration parameters were required to represent the constitutive behavior. Since Abaqus only allows for the input of one set of parameters to define the JC model, we implement the plasticity model through tabular data obtained from the calibrated JC model.

To calibrate the JC model, tensile tests were performed on 2 mm thick dog-bone specimens over a range of strain rates from $6.8 \cdot 10^{-5}$ to $7 \cdot 10^{-2}\ s^{-1}$; details regarding the testing procedure can be found in Gamble et al. (2013). The measured stress–strain curves are shown in Fig. 2(a). The mechanical properties and model parameters (obtained from curve fitting) are listed in Table 2. Two sets

Table 2
Properties of the 4130 steel layers.

Property	Value	Domain
ρ (kg/m^3)	7830	
E (GPa)	200	
v	0.3	
A (MPa)	115.5	$\bar{\varepsilon}^{pl} \leqslant 0.2$
B (MPa)	617	$\bar{\varepsilon}^{pl} \leqslant 0.2$
n	0.1939	$\bar{\varepsilon}^{pl} \leqslant 0.2$
A (MPa)	0	$\bar{\varepsilon}^{pl} > 0.2$
B (MPa)	581.53	$\bar{\varepsilon}^{pl} > 0.2$
n	0.0178	$\bar{\varepsilon}^{pl} > 0.2$
C	0.013	
$\dot{\varepsilon}_o$ (1/s)	6.8×10^{-4}	
m	1	
T_{room} (K)	300	
T_{melt} (K)	1800	
c_p (J/kg K)	450	

of the parameters A, B and n – one for small strains and one for large strains – were determined from the stress–strain curves at a strain rate of $\dot{\varepsilon}_o = 6.8 \cdot 10^{-4}\ s^{-1}$ In the regime preceding necking ($\bar{\varepsilon}^{pl} \leqslant 0.2$), the data were used to compute the true stress–strain response and the parameters A, B and n were determined by fitting these results. The second set (for $\bar{\varepsilon}^{pl} > 0.2$) was determined from the post-necking regime by fitting the nominal stress–strain curves with finite element calculations. The parameters were selected to ensure continuity in the stress–strain response at the transition strain (*i.e.*, at the onset of necking). The strain rate sensitivity parameter C was determined by performing a linear fit to the strain rate sensitivity data (Fig. 2(b)). The flow stress is assumed to decrease linearly between room temperature and the melting point ($m = 1$), as done in previous studies (Johnson and Cook, 1985; Dabboussi and Nemes, 2005). Again, 90% of the energy from plastic deformation is assumed to be converted into heat.

Following Gamble et al. (2013), failure initiation in the metal layers is assumed to occur at a critical equivalent plastic strain: either 1.2, for stress triaxialities above −0.3, or 10, for lower triaxialities. The lower failure strain corresponds to that for uniaxial tensile loading, obtained from area reduction measurements on tensile test

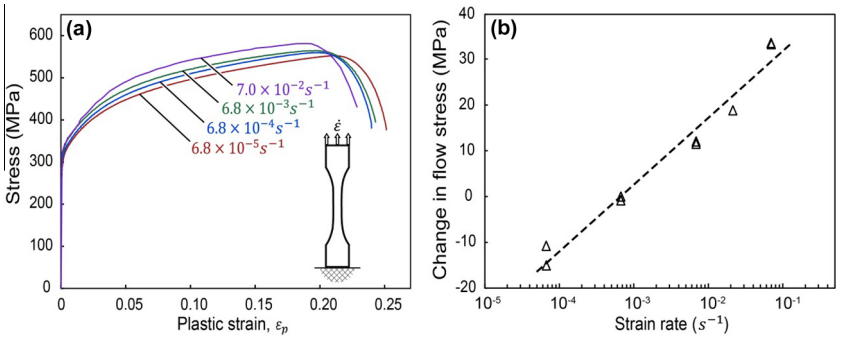

Fig. 2. Tensile test results for 4130 steel: (a) engineering stress–strain curves at various strain rates; (b) effects of strain rate on the flow stress relative to that at a reference strain rate of $6.8 \times 10^{-4}\ s^{-1}$ at a plastic strain of 0.1. The dashed line in (b) is a linear fit to the data used to determine the rate sensitivity parameter C.

specimens. Once the critical strain is reached in an element, its strength is reduced linearly with further element extension, reaching zero at an extension of 5 μm (corresponding to a maximum additional strain of 0.05 for a 100 μm element size); a small, yet finite, extension value is used to avoid dynamic instabilities associated with an instantaneous drop in stress at a material point. At this point the element is deleted. In the front facesheet, this criterion allows for deletion of the highly sheared elements on the periphery of the penetrating impactor, while preventing elimination of the highly confined elements directly beneath the impactor; in this way the losses in mass that result from element deletion were minimized. Although the highly confined elements in the front facesheet do not experience damage until unrealistically high plastic strains, their strength is greatly reduced by thermal softening at early times after impact. Consequently, the computed results for the back-face displacement are found to be *insensitive* to the input failure parameters of the front facesheet. During the penetration process, the elements in the back facesheet experience tension and therefore fail at the lower critical strain. The onset of element erosion in the back facesheet is used as an indication of penetration initiation. No attempt is made to model the complete rupture and penetration process that ensues.

2.2.3. Ceramic layer

The deformation and fracture behavior of the ceramic is represented by the extended DE model, which has been implemented in Abaqus/Explicit as a user subroutine VUMAT. The model is described in full in Deshpande et al. (2011) and its key features are summarized in Appendix in Gamble et al. (2011). In summary, the model incorporates the three principal inelastic deformation mechanisms: lattice plasticity, microcracking and granular plasticity. The state of microcracking is captured through a damage parameter, D, defined by

$$D = \frac{4}{3}\pi(l + \alpha a)^3 \eta, \tag{3}$$

where l is the length of the wing cracks emanating from a penny-shaped flaw of radius a, η is the number of flaws per unit volume and α is a crack orientation factor (0.707). Once D reaches unity, a Drucker–Prager constitutive law for granular plasticity is utilized to describe the subsequent flow response of the comminuted material. A rate-dependent von Mises model is used to capture lattice plasticity at low stress triaxialities both before and after comminution.

The DE model parameters used in the present study (Table 3) are the same as those used in a preceding study (Gamble et al., 2013), with one exception: Whereas the soil friction angle, ω, and the associated dilatation angle, ψ, were progressively diminished with strain in the previous study (in order to match experimental results at higher velocities), both ω and ψ were held fixed in the present study. With this choice of parameters, we find that the numerical predictions of the back facesheet deflection profile are in close agreement with experimental results in the velocity domain of present interest, as discussed in the following section.

Table 3
Deshpande–Evans model parameters for Corbit 98 armor alumina (from Gamble et al. (2013)).

Parameter	Selected value	Description
ρ (kg/m^3)	3810	Density
ν	0.239	Poisson's ratio
E (GPa)	366	Young's modulus
$d(\mu m)$	3.0	Grain diameter
σ_y (GPa)	5.75	Yield stress
K_{Ic} (MPa$\sqrt{\text{m}}$)	3.0	Fracture toughness
M	0.1	Strain hardening exponent
m	30	Crack growth rate sensitivity exponent
n	34	Strain rate dependence exponent
$\dot{l}_o$ (m/s)	0.01	Reference crack growth rate
ε_o	0.002	Reference strain
$\dot{\varepsilon}_o$ (1/s)	0.001	Reference plastic strain rate
g_1	0.5	Normalized flaw size
g_2	6	Normalized flaw spacing
α	0.707	Crack orientation factor
β	0.45	Parameter to ensure 2-D compatibility
γ	6	Crack geometry factor
μ	0.75	Crack coefficient of friction
$\dot{\varepsilon}_t$ (1/s)	10^6	Transition shear strain rate
ω	60°	Soil friction angle
σ_c (MPa)	1	Soil uniaxial compressive strength
x_d	5	Soil transition exponent
$\dot{\varepsilon}_{cut\text{-}off}$ (1/s)	2×10^6	Soil transition strain rate
ψ	15°	Dilatation angle

2.3. Validation of FE model

The predictive capability of the FE model was assessed through comparisons with the impact experiments reported in Gamble et al. (2013). The assessment is made on the basis of the deflection profiles of the back facesheets for a reference trilayer subject to ballistic impact by a steel sphere with a mass of 1.49 g. The reference trilayer has a 1 mm thick steel front facesheet, a 6 mm thick alumina core and a 2 mm thick steel back facesheet. Its total areal density is $\bar{\rho} = 46.35$ kg m^{-2}.

Simulation results and experimental measurements of the permanent back-face displacement profiles are shown in Fig. 3 for three impact velocities: 1160, 1273 and 1438 m/s. Excellent agreement is obtained between the simulations and the experiments over the pertinent range of impact velocities. These comparisons, combined with previous studies on the ceramic alone (Deshpande et al., 2011; Gamble et al., 2011; Compton et al., 2013), provide validation of the FE model used in the ensuing parametric study.

2.4. Parametric study of target design

A parametric study was performed to explore the performance of bilayers and trilayer targets over a broad design space. Targets are subjected to normal impact at 1000 and 1250 m/s; for the majority of target configurations, these velocities are below the ballistic limit. The areal density is given by

$$\bar{\rho} = \rho_m(t_{m,f} + t_{m,b}) + \rho_c t_c, \tag{4}$$

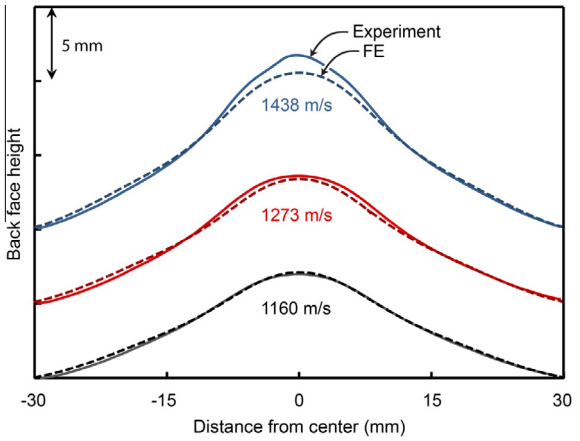

Fig. 3. Post-impact displacement profiles of the back face for the reference trilayer system ($\bar{m} = 1,\ \bar{m} = 0.5$) at three impact velocities.

where ρ_m and ρ_c are the mass densities of the metal (4130 steel) and the ceramic (alumina), respectively. All systems have an areal density that matches that of the reference trilayer, notably $\bar{\rho} = 46.35\ \text{kg m}^{-2}$.

In addition to areal density, the targets are characterized by two dimensionless parameters: (i) the ratio of ceramic mass, m_c, to metal mass, m_m, denoted $\bar{m}$ (*i.e.*, $\bar{m} = \rho_c t_c / \rho_m (t_{m,f} + t_{m,b})$); and (ii) the ratio $\bar{t}$ of thicknesses of the front and back facesheets ($\bar{m} = t_{m,f}/t_{m,b}$). The configurations are limited to those having mass and thickness ratios in the ranges of [0,2] and [0,1], respectively. (In this context, the reference trilayer used for validation in the preceding section is characterized by $\bar{m} = 1.0$ and $\bar{m} = 0.5$ the center point of the design space).

A schematic representation of the design space is shown in Fig. 4. Three target types are identified in this space: (i) monolithic steel (along the vertical axis, at $\bar{m} = 0$); (ii) bilayers of alumina backed by steel facesheets (along the horizontal axis, at $\bar{m} = 0$); and (iii) steel–alumina–steel trilayers (within the space having $\bar{m} \neq 0$ and $\bar{m} \neq 0$). Also illustrated in the figure are the effects of $\bar{m}$ and $\bar{t}$ on the trilayer configuration. For instance, reducing $\bar{t}$ at fixed $\bar{m}$ leads to a reduction in the thickness of the front metal facesheet $t_{m,f}$ and an increase in the back metal facesheet $t_{m,b}$; the thickness of the ceramic layer t_c is unaffected. Alternatively, increasing $\bar{m}$ at fixed $\bar{t}$ leads to a reduction in the mass of the metal facesheets and a corresponding increase in the mass of the ceramic layer. For specified values of $\bar{i}$, $\bar{m}$, $\bar{\rho}$, ρ_m and ρ_c, the absolute layer thicknesses can be expressed as

$$t_{m,f} = \frac{\bar{t}\bar{\rho}}{\rho_m(1+\bar{m})(1+\bar{t})}, \tag{5}$$

$$t_c = \frac{\bar{m}\bar{\rho}}{\rho_c(1+\bar{m})}, \tag{6}$$

and

$$t_{m,b} = \frac{\bar{\rho}}{\rho_m(1+\bar{m})(1+\bar{t})}. \tag{7}$$

The total target thickness is:

$$t_{tot} = t_{m,f} + t_{m,b} + t_c = \frac{(\rho_c + \rho_m\bar{m})\bar{\rho}}{\rho_c\rho_m(1+\bar{m})}. \tag{8}$$

Note that the total thickness depends on $\bar{m}$ but not $\bar{t}$.

3. Numerical results and discussion

3.1. Analysis of a representative simulation

We begin by presenting and analyzing the results of a representative impact simulation; the same general features are in all simulations. The representative results are shown in Fig. 5. The target is a trilayer with $\bar{m} = 0.8$ and $\bar{m} = 0.6$ impacted at 1000 m/s. Images from this simulation at 3, 30 and 300 μs after initial impact reveal the deformation response of the target and the projectile (Fig. 5(a)). In the first few microseconds after contact, large impact stresses are generated, resulting in significant plastic deformation of the projectile and, beneath the projectile, erosion of the front facesheet. Meanwhile, the ceramic tile begins to damage, due to the growth of microcracks; cone and circumferential cracks also form at the

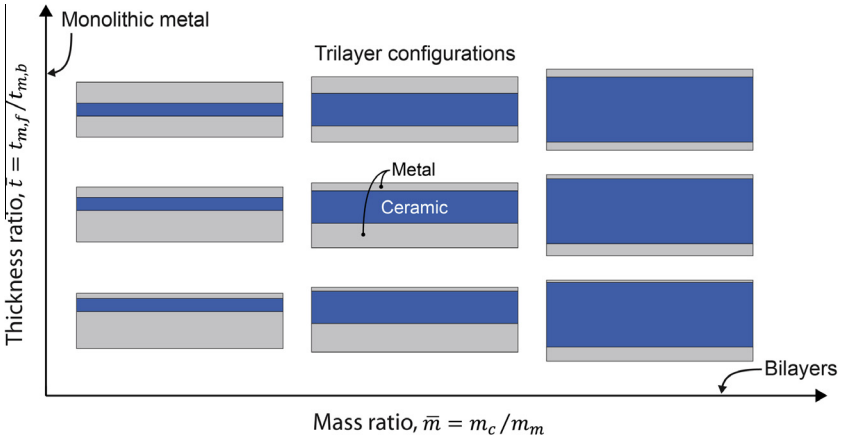

Fig. 4. Schematic of the design space, showing effects of mass and thickness ratios on target configuration for a constant areal density.

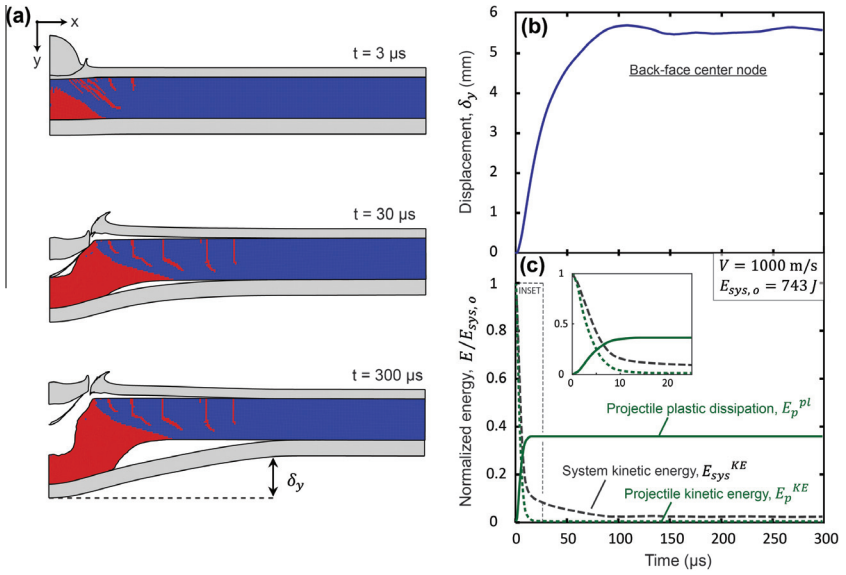

Fig. 5. Representative simulation results for a trilayer with $\bar{m} = 0.8$ and $\bar{m} = 0.6$, impacted at 1000 m/s. (a) Images at 3, 30 and 300 μs after initial impact, showing the extent of deformation and damage. The red and blue regions indicate fully damaged and undamaged ceramic material, respectively (see colors online). Histories of (b) peak back-face deflection and (c) pertinent energies. (For interpretation of the references to color in this figure legend, the reader is referred to the web version of this article.)

impact site. (Because of axial symmetry, radial cracking is not permitted.) Due to the reflection of stress waves from the interface between the ceramic and the back facesheet, a damage region grows from this interface toward the impact face; this is already visible at 3 μs after impact. By 5 μs after impact, the latter damage zone has linked up with the approaching cone crack. At approximately 17 μs, the projectile is arrested. Thereafter, the remaining kinetic energy is dissipated through plastic deformation in the back facesheet.

At the end of the simulations, the maximum permanent deflection of the back face is measured and the energy dissipated by the target through inelastic deformation is determined. Simulations proceed until a time at which the kinetic plus elastic strain energy of the system E_{sys}^{KE} reaches a low, constant value (Fig. 5(c)), allowing for estimation of the permanent back-face deflection, on the axis of symmetry (Fig. 5(b)). (The kinetic energy of the system never reaches zero in the simulation because energy can only be dissipated through inelastic deformation and thus some elastic strain energy remains.) In all simulations, the final kinetic energy in the system is less than 5% of the initial kinetic energy. In the representative case shown in Fig. 5, the back face exhibits a permanent displacement of ~5.6 mm and 36% of the initial kinetic energy is dissipated through plasticity in the projectile. From energy conservation, the energy dissipated by the target through inelastic deformation E_t^{inelas} is

$$E_t^{inelas} = \Delta E_{sys}^{KE} - E_p^{pl}, \tag{9}$$

where E_p^{pl} is the energy dissipated by plastic deformation in the projectile and ΔE_{sys}^{KE} is the change in kinetic and elastic strain energy in the system.

Since the final kinetic plus elastic strain energy in the system is a small fraction (<5%) of the initial kinetic energy, the energy dissipated by the target is approximately equal to the difference between the initial energy and the energy dissipated through plasticity in the projectile (*i.e.*, $E_t^{inelas} \approx E_{sys,o} - E_p^{pl}$). In other words, since the impact velocity is below the ballistic limit, nearly all of the initial energy in the projectile is dissipated through inelastic deformation of the projectile and the target. The energy dissipated by the target occurs through a combination of lattice plasticity in the metal layers and, in the ceramic layer, lattice plasticity, microcracking and granular plasticity. From the results plotted in Fig. 5(c), the energy dissipated by the target is about 60% of the initial projectile kinetic energy.

3.2. Effects of target design on permanent deflection

Here we analyze the results from the parametric study with emphasis on permanent back-face deflection, δ_y. The results are presented in Fig. 6 as contour maps in $\bar{m}$–$\bar{t}$ space, for impact velocities of (a) 1000 and (b) 1250 m/s. Each circle on the maps represents an individual target configuration analyzed by finite elements. Failure initiation boundaries (indicated by the dashed lines) separate the surviving targets from those penetrated. (Recall that a target is deemed to have been penetrated (failed) when the peak equivalent plastic strain in the back facesheet reaches a critical value.) The deflection of penetrated targets is not recorded since element deletion usually occurs on or near the axis of symmetry, where target deflection is monitored. The contour plots were created in MATLAB® R2011b using a triangular linear interpolation scheme.

The general trends in Fig. 6(a) and (b) are qualitatively similar to one another and show the effects of target design

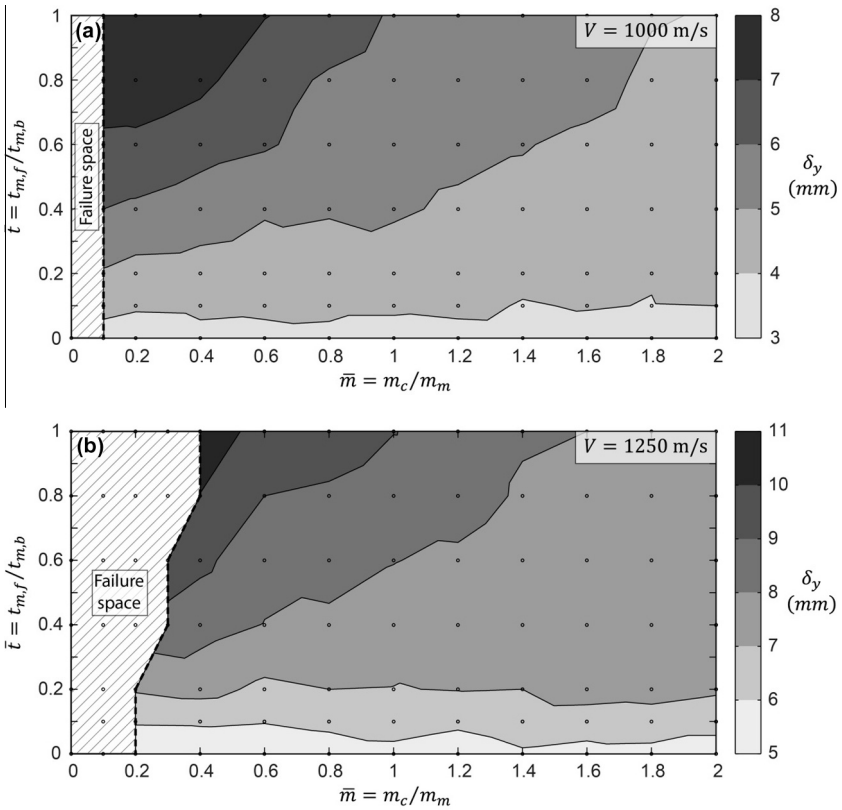

Fig. 6. Contour plots showing the effects of mass and thickness ratio on permanent back face deflection for impact velocities of (a) 1000 and (b) 1250 m/s. The circles indicate the designs that were analyzed by FE. The dashed lines represent the approximate failure initiation boundaries.

on permanent deflection. The trends are summarized as follows. First, for targets of a given (non-zero) $\bar{t}$, deflection decreases with increasing $\bar{m}$, where targets with low $\bar{t}$ are less sensitive to changes in $\bar{m}$ than targets with high $\bar{t}$. Second, for targets of a given $\bar{m}$, permanent deflection decreases with decreasing $\bar{t}$, where targets with large $\bar{m}$ are less sensitive to changes in $\bar{t}$ than targets with low $\bar{m}$. Accordingly, of the target designs, the bilayers ($\bar{m} = 0$ and $\bar{m} > 0$) are best. Surprisingly, for a given impact velocity, the deflections of all bilayers are roughly equal (~3–4 mm for impact at 1000 m/s and ~5–6 mm for impact at 1250 m/s), provided $\bar{m}$ exceeds a critical value. Otherwise, at very low $\bar{m}$, penetration ensues.

Additional insights into the beneficial effects of the ceramic to target survivability can be gleaned by comparing the responses of the monolithic steel target and the steel–ceramic bilayers. At 1000 m/s, the monolithic steel target is penetrated by the projectile and forms a plug which exits the target, along with the projectile, at 140 m/s (Fig. 7, left). Penetration occurs by shear plugging in a localized region around the periphery of the contact when the material in this region reaches the critical failure strain. Furthermore, we note that the localization appears to occur shortly after contact, although the shear band is formed after more extensive deformation. In contrast, when a small amount of steel is replaced by an equivalent mass of ceramic ($\bar{m} = 0.1$), penetration does not occur (Fig. 7, right). Evidently the thin ceramic face is sufficient to blunt the projectile, spread the impact load over a larger area and prevent the formation of localized shear zones in the steel backsheet. Additionally, by comparing the failure spaces in Fig. 6(a) and (b), we note that the target designs that are nearest to the failure space at the lower velocity (*i.e.,* those with low $\bar{m}$) experience failure at the higher velocity case. This is particularly true for structures with large $\bar{t}$. The implication is that the proximity of a target design to the failure initiation boundary is indicative of its vulnerability to penetration at higher velocities, even when the permanent deflections are the same.

3.3. Effects of target design on energy dissipation

The effects of target design on the energy dissipated by the target E_t^{inelas}, normalized by the initial kinetic energy $E_{sys,o}$, are shown in Fig. 8 for the two impact velocities. The dashed white lines superimposed on Fig. 8(a) and (b) are the failure initiation boundaries taken from Fig. 6(a) and (b), respectively. Recall that, since the final kinetic energy plus elastic strain energy of the system is a small fraction of its initial energy (<5%), the energy not dissipated in the target is approximately equal to the energy dissipated in the projectile (Eq. (9)).

The results in Fig. 8 shows that: (i) for a prescribed $\bar{t}$, the amount of energy dissipated by the target decreases with

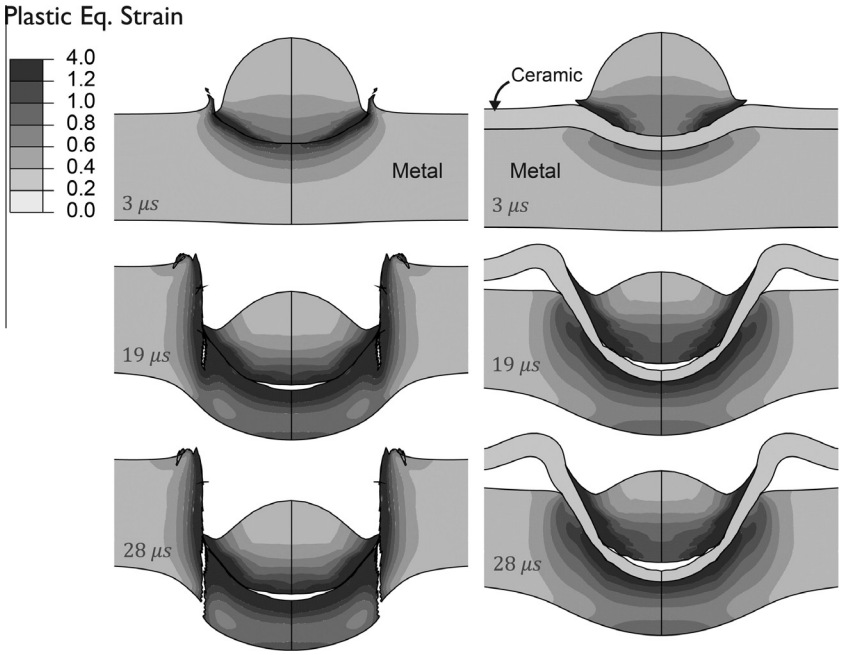

Fig. 7. Plots showing the penetration response and deformation of the (left) monolithic metal target and a (right) ceramic–metal bilayer ($\bar{m} = 0.1$) impacted at 1000 m/s. We infer that the ceramic protects the underlying metal layer by blunting the projectile and spreading the impact load, which can prevent the formation of localized shear bands that lead to plugging.

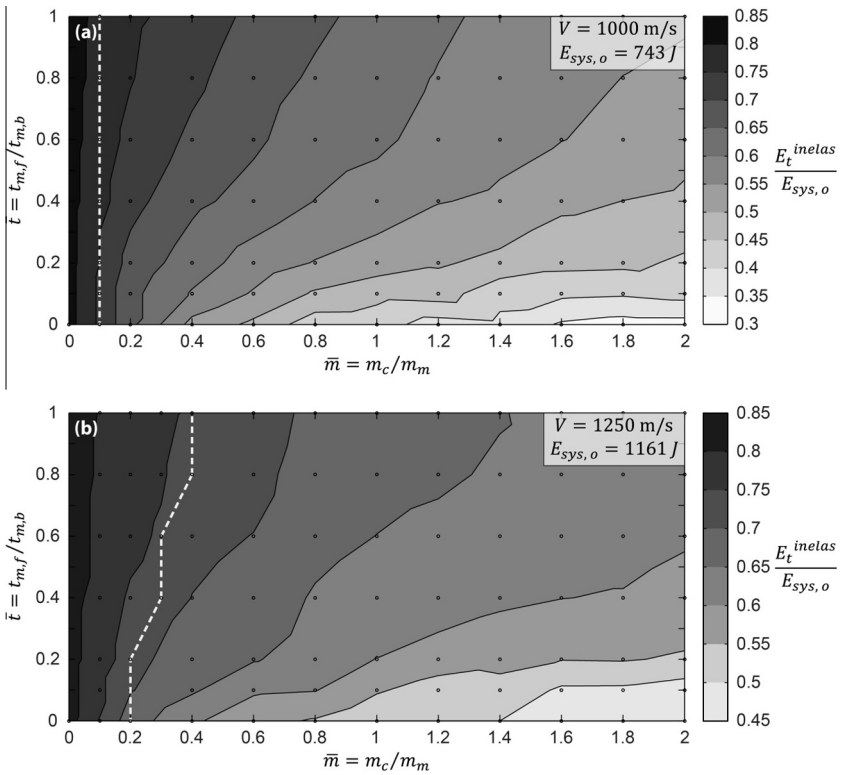

Fig. 8. Contour plots showing the effects of mass and thickness ratios on energy dissipated in the target, normalized by the initial kinetic energy of the projectile, for impact velocities of (a) 1000 and (b) 1250 m/s. The white dashed lines are the failure initiation boundaries, from Fig. 6.

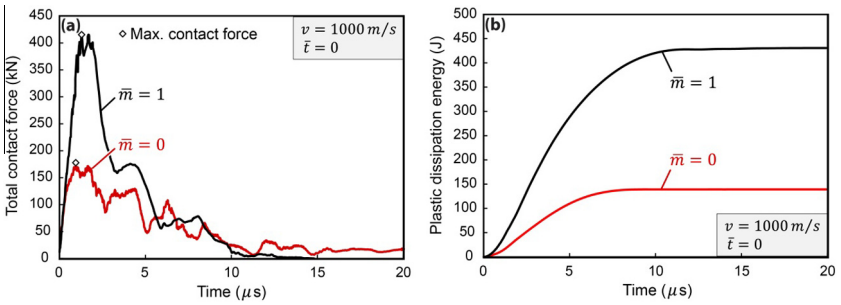

Fig. 9. Temporal evolution of (a) total contact force and (b) plastic dissipation in the projectile for impact velocity of 1000 m/s against the monolithic metal target ($\bar{m} = 0$) and a bilayer ($\bar{m} = 1$). The results were recorded every 10 ns and a simple moving average was applied to the force data to reduce numerical noise. The bilayer is able to support larger contact forces, which, in turn, causes increased levels of energy dissipation in the projectile.

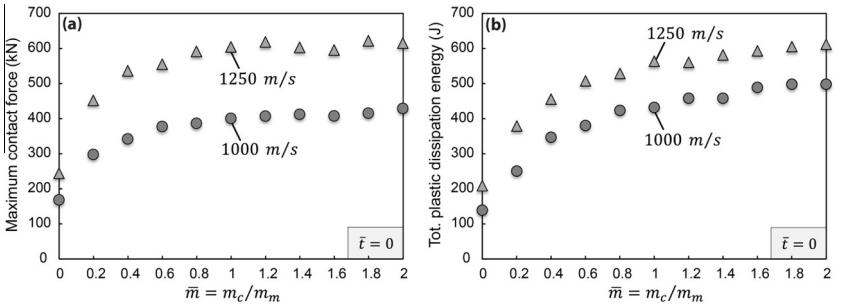

Fig. 10. Effect of mass ratio $\bar{m}$ and impact velocity on (a) maximum contact force and (b) plastic dissipation in the projectile for a series of bilayers. Both parameters appear to approach an asymptote at high values of $\bar{m}$ (>1).

increasing $\bar{m}$; and (ii) for a prescribed (non-zero) $\bar{m}$, the energy dissipated by the target decreases with decreasing $\bar{t}$. Accordingly, of the target designs within the limits of the design space, the monolithic steel dissipates the greatest amount of energy and the bilayer with the largest mass ratio ($\bar{m} = 2.0$) dissipates the least. Conversely, the amount of energy dissipated in the projectile is lowest for the monolithic steel target and greatest for the bilayer with $\bar{m} = 2.0$. Moreover, similarities in the shapes of the failure initiation boundaries and those of the underlying energy contours suggests that the energy dissipated in the target may provide a useful measure of its vulnerability to penetration. Thus, in combination with the permanent deflection contour maps, the two metrics yield a more complete description of ballistic performance than either one of the two alone. A further implication is that targets should be designed to maximize energy dissipation *within the projectile itself* and therefore minimize the energy that must be dissipated within the target.

Projectile impact on a hard ceramic, relative to impact on a metal, results in the generation of larger forces that increase the level of deformation in the projectile and thus causing it to dissipate a greater fraction of its initial kinetic energy through projectile deformation. This effect can be seen in Figs. 9 and 10. Fig. 9 gives the temporal variations in (a) force and (b) plastic dissipation in the projectile due to impact on a monolithic metal target ($\bar{m} = 0$) and on a ceramic–metal bilayer with $\bar{m} = 1$. We note that the maximum force due to impact on the bilayer, which occurs in the first 1–2 μs, is more than twice the maximum force that is generated during impact on the monolithic metal target (Fig. 9(a)). Consequently, the energy dissipated by the projectile during impact on the bilayer is more than twice the energy dissipated during impact on the metal target. Furthermore, the effects of bilayer mass ratio and impact velocity on the maximum contact force and the plastic dissipation energy in the projectiles are shown in Fig. 10. As expected, for a given $\bar{m}$, both the contact force and the energy dissipation within the projectile increase in tandem with increasing impact velocity. Moreover, both parameters appear to approach asymptotic values for $\bar{m} \geqslant 1$, indicating diminishing returns with further increases in ceramic content.

4. Summary and conclusions

A numerical parametric study using finite element analysis has been performed to investigate the effects of target design on ballistic performance of unbonded, thin ceramic–metal bilayers and trilayers of equivalent areal density, subject to normal impact by a steel sphere at velocities of 1000 and 1250 m/s. Comparisons with select experimental measurements of the permanent back-face deflection – the key performance metric – were used to validate the material models. It is noted that the conclusions of this study may not extend to scenarios where the impact event and/or projectile-target system are different than those described in this paper.

The results of the parametric study reveal the following trends in ballistic performance as measured by the extent of back-face deflection after impact:

(i) The ceramic–metal bilayer design exhibits the highest ballistic resistance (lowest back-face deflection after impact).
(ii) For bilayers, ballistic resistance is nearly independent of ceramic/metal mass ratio; however, depending on impact velocity, mass ratio must be above a critical value to prevent penetration.
(iii) Removing metal from the steel backsheet and placing it on the impacted face (forming a trilayer) reduces ballistic resistance.

Penetration of the back facesheet, defined by either the attainment of a critical strain or a sufficient loss in strength due to adiabatic heating, is found to correlate with high levels of energy dissipation in the target. This correlation suggests that the emphasis of armor designs should be on maximizing the energy dissipated within the projectile itself, thereby minimizing the energy that must be dissipated within the target. Accordingly, effective armor designs, characterized by small amounts of back-face deflection and low vulnerability to penetration, would have high ceramic/metal mass ratios with the vast majority of metal on the back face.

Acknowledgments

This research was supported by the Army Research Laboratory (ARL) through the Johns Hopkins University Collaborative Program for the Multiscale Modeling and Design of Materials for Extreme Dynamic Environments. Additionally, we acknowledge computing support from the Center for Scientific Computing at the CNSI and MRL: an NSF MRSEC (DMR-1121053) and NSF CNS-0960316. Finally, we gratefully acknowledge Louis Perez of the University of California, Santa Barbara for evaluating and providing valuable feedback on the figures in this paper.

References

Bao, Y., Wierzbicki, T., 2004. On fracture locus in the equivalent strain and stress triaxiality space. Int. J. Mech. Sci. 46, 81–98. http://dx.doi.org/10.1016/j.ijmecsci.2004.02.006.

Ben-Dor, G., Dubinsky, A., Elperin, T., Frage, N., 2000. Optimization of two component ceramic armor for a given impact velocity. Theor. Appl. Fract. Mech. 33, 185–190.

Ben-Dor, G., Dubinsky, A., Elperin, T., 2005. Optimization of two-component composite armor against ballistic impact. Compos. Struct. 69, 89–94. http://dx.doi.org/10.1016/j.compstruct.2004.05.014.

Ben-Dor, G., Dubinsky, A., Elperin, T., 2009. Improved Florence model and optimization of two-component armor against single impact or two impacts. Compos. Struct. 88, 158–165. http://dx.doi.org/10.1016/j.compstruct.2008.02.015.

Compton, B.G., Gamble, E.A., Zok, F.W., 2013. Failure initiation during impact of metal spheres onto ceramic targets. Int. J. Impact Eng. 55, 11–23. http://dx.doi.org/10.1016/j.ijimpeng.2012.12.002.

Dabboussi, W., Nemes, J.A., 2005. Modeling of ductile fracture using the dynamic punch test. Int. J. Mech. Sci. 47, 1282–1299. http://dx.doi.org/10.1016/j.ijmecsci.2005.01.015.

Deshpande, V.S., Evans, A.G., 2008. Inelastic deformation and energy dissipation in ceramics: a mechanism-based constitutive model. J. Mech. Phys. Solids 56, 3077–3100. http://dx.doi.org/10.1016/j.jmps.2008.05.002.

Deshpande, V.S., Gamble, E.A., Compton, B.G., McMeeking, R.M., Evans, A.G., Zok, F.W., 2011. A constitutive description of the inelastic response of ceramics. J. Am. Ceram. Soc. 94, s204–s214. http://dx.doi.org/10.1111/j.1551-2916.2011.04516.x.

Dey, S., Børvik, T., Hopperstad, O.S., Langseth, M., 2007. On the influence of constitutive relation in projectile impact of steel plates. Int. J. Impact Eng. 34, 464–486. http://dx.doi.org/10.1016/j.ijimpeng.2005.10.003.

Fawaz, Z., Behdinan, K., Xu, Y., 2006. Optimum design of two-component composite armours against high-speed impact. Compos. Struct. 73, 253–262. http://dx.doi.org/10.1016/j.compstruct.2005.01.037.

Gamble, E.A., Compton, B.G., Deshpande, V.S., Evans, A.G., Zok, F.W., 2011. Damage development in an armor ceramic under quasi-static indentation. J. Am. Ceram. Soc. 94, s215–s225. http://dx.doi.org/10.1111/j.1551-2916.2011.04472.x.

Gamble, E.A., Compton, B.G., Zok, F.W., 2013. Impact response of layered steel–alumina targets. Mech. Mater. 60, 80–92. http://dx.doi.org/10.1016/j.mechmat.2013.01.008.

Goncalves, D., De Melo, F., 2004. Analysis and investigation of ballistic impact on ceramic/metal composite armour. Int. J. Mach. Tools Manuf. 44, 307–316. http://dx.doi.org/10.1016/j.ijmachtools.2003.09.005.

Hetherington, J., Rajagopalan, B., 1991. An investigation into the energy absorbed during ballistic perforation of composite armours. Int. J. Impact Eng. 11, 33–40.

Hetherington, J., 1992. The optimization of two component composite armours. Int. J. Impact Eng. 12, 409–414.

Johnson, G., Cook, W., 1983. A constitutive model and data for metals subjected to large strains, high strain rates and high temperatures. In: Proc. Seventh Int. Symp. Ballist.

Johnson, G., Cook, W., 1985. Fracture characteristics of three metals subjected to various strains, strain rates, temperatures and pressures. Eng. Fract. Mech. 21.

Lopez-Puente, J., Arias, A., Zaera, R., Navarro, C., 2005. The effect of the thickness of the adhesive layer on the ballistic limit of ceramic/metal armours. An experimental and numerical study. Int. J. Impact Eng. 32, 321–336, doi:http://dx.doi.org/10.1016/j.ijimpeng.2005.07.014.

Sarva, S., Nemat-Nasser, S., McGee, J., Isaacs, J., 2007. The effect of thin membrane restraint on the ballistic performance of armor grade ceramic tiles. Int. J. Impact Eng. 34, 277–302. http://dx.doi.org/10.1016/j.ijimpeng.2005.07.006.

Shi, J., Grow, D., 2007. Effect of double constraints on the optimization of two-component armor systems. Compos. Struct. 79, 445–453. http://dx.doi.org/10.1016/j.compstruct.2006.02.015.

Stout, M., Follansbee, P., 1986. Strain rate sensitivity, strain hardening, and yield behavior of 304L stainless steel. J. Eng. Mater. Technol. 108, 344–353.

Wilkins, M., Honodel, C., Sawle, D., 1967. An Approach to the Study of Light Armor. University of California, Lawrence Radiation Laboratory.

Wilkins, M., 1978. Mechanics of penetration and perforation. Int. J. Eng. Sci. 16, 793–807.

Zaera, R., Sánchez-Gálvez, V., 1998. Analytical modelling of normal and oblique ballistic impact on ceramic/metal lightweight armours. Int. J. Impact Eng. 21, 133–148.

Zerilli, F., Armstrong, R., 1987. Dislocation-mechanics-based constitutive relations for material dynamics calculations. J. Appl. Phys. 5000, 1816–1825.